Science Advances
AAAS

Supplementary Materials for

Wave ripples formed in ancient, ice-free lakes in Gale crater, Mars

Claire A. Mondro *et al.*

Corresponding author: Claire A. Mondro, cmondro@caltech.edu

Sci. Adv. **11**, eadr0010 (2025)
DOI: 10.1126/sciadv.adr0010

This PDF file includes:

Supplementary Text S1 to S4
Figs. S1 to S6
Tables S1 and S2
References

Supplementary Text

S1. Instruments and Imaging

Curiosity imaged the Prow outcrop in detail from multiple positions, including up-close orthogonal views of the cm-scale ripples in two locations. All Mast Camera (Mastcam) image mosaics included in this manuscript were processed by Malin Space Science Systems (MSSS) using the routine workflow that is applied to all Mastcam mosaics, which includes standardized radiometric and geometric calibrations and a color balance correction as part of the mosaicking process (*58*).

Morphology measurements on Mars Hand Lens Imager (MAHLI) and Chemistry & Camera (ChemCam) long distance Remote Micro Imager (LD-RMI) image data (*59*) were made in pixels and converted to distances by the pixel resolution of each image. Pixel resolutions of the MAHLI images were calculated from the image scale bar that is provided on images processed by the MAHLI team. Pixel resolutions of the LD-RMI images were calculated from the ChemCam camera instantaneous field of view (iFOV) and the distance from camera to target.

The orientation of ripple crests was estimated using Navigation Camera (Navcam) stereomesh data products (*60*). Ripple crest orientations were estimated along the top of each outcrop in plan view (uncertainty of ±10°). The orientation of the Amapari Marker Band (AMB) and Prow outcrops at the locations where ripples were observed was measured on georeferenced High Resolution Imaging Science Experiment (HiRISE) orbiter image data (uncertainty of ±10°) displayed in the Multi-Mission Geographic Information System (MMGIS) program (*61-63*).

Identification and measurement of grain size was performed using MAHLI image data. The lower limit of resolution of MAHLI images in ~60 µm/pixel (*36*) and the smallest grain size that is confidently detectable in these images is ~180 µm in diameter, or the size of fine sand. If no grains are detectable in MAHLI images, the grain size is assumed to be < 180 µm.

S2. Ripple Measurements

AMB grains are not detectable in MAHLI images but must be large enough to form ripples (i.e. larger than silt-size). Therefore, the grain size of the AMB ripples is assumed to be between 60 – 180 µm, or very fine to fine sand. Individual sand grains are visible in the MAHLI images of the Sumuru target at the Prow (Fig S4). Point counting within a subset of the highest-resolution image produced a grain size range of 140 – 1000 µm (D_{50} = 389 µm; medium sand).

Ripple crest orientation was only visible and measurable in one location along the Prow and at two adjacent locations at the AMB. The Prow ripple crest orientation was measured within the same layer that contains the ripples used for morphologic analysis, but ~2 m away from where ripple morphology was measured. The AMB ripple crest orientation was measured along the top of the uppermost ripple layer ~4 m away from the ripples used for morphologic analysis, along which a visual assessment of outcrop character indicates that the ripple orientation is largely consistent. At both the Prow and AMB locations, ripple crest orientation is approximately orthogonal to outcrop orientation (Tables S1, S2).

Ripple wavelength (λ) is defined as the horizontal distance between adjacent ripple crests, measured parallel to bedding. Wavelength measurements, including mean and range for each ripple population, are included in Tables S1 and S2. Because ripple crests at both the AMB and the Prow are approximately orthogonal to the orientation of the outcrop, the measured wavelength is very similar to the true wavelength. Non-orthogonal wavelength measurements would increase the measured wavelength (λ_m) relative to the true wavelength (λ_t). Assuming a maximum potential uncertainty in orientation measurements of up to 20°, we calculated the percent change in wavelength to assess the effect of the orientation uncertainties on wavelength measurements. A 20° change in the angle between ripple crest and outcrop orientation produces a λ_t that is 6% smaller than the λ_m, where

$$\cos(20°) = {}^{\lambda_t}/_{\lambda_m} \tag{1}$$

and therefore

$$\lambda_t = \lambda_m \times 0.94. \tag{2}$$

For the AMB ripples, this correction shifts the wavelength range to 3.6 cm – 5.0 cm (mean λ_t = 4.18 cm). For the Prow ripples, this correction shifts the wavelength range to 3.27 cm – 5.5 cm (mean λ_t = 4.4 cm). The corrected wavelengths do not contribute to any significant change in the morphology interpretation of the ripples. Because the difference is small and the corrections are based on the maximum combined uncertainty from the orientation measurements, where the true correction within that range is unknown, we use the measured wavelengths throughout the manuscript text to describe ripple morphology.

The symmetry index of a ripple is defined as the horizontal distance from trough to crest on the left side, divided by the horizontal distance from trough to crest on right side, where distances are measured laterally, parallel to bedding. Symmetry index is often measured as a ratio of the stoss side to lee side (*39*) but in the case of the AMB and the Prow, the ripples are symmetric enough that the stoss and lee sides are not immediately discernible. Therefore, we kept the measurements consistent as left over right within the view angle towards the outcrop. Keeping the ratio consistent in this way also allowed us to confirm that there is no consistent direction of asymmetry.

Wave ripples have a symmetry index of < 1.5, combined flow ripples have a symmetry index between 1.5 and 3.0, and current-dominated ripples have a symmetry index >3.0 (*39*). These values assume the symmetry index is measured as the ratio of stoss to lee side (where the minimum possible value is 1.0). When stoss and lee sides are not differentiated, wave ripples have a symmetry index between 0.7 and 1.5. Symmetry index measurements for the AMB and Prow ripples, including range and mean for each ripple population, are included in Tables S1 and S2. Symmetry index values do not directly correspond with individual ripple wavelengths because wavelength is measured crest to crest and symmetry defines a single ripple as trough to trough.

Ripple height (h) is defined as the maximum vertical distance from trough to crest, measured perpendicular to the ripple layer. Ripple aspect ratio (h/λ) was calculated for each corresponding ripple wavelength and height (Tables S1, S2). The aspect ratio would also be affected by uncertainty in the wavelength measurements as a result of uncertainty in the orientation measurements. If λ_t is up to 6% smaller than λ_m, the true corrected aspect ratio (h/λ_t) would be up to 6% larger than the measured aspect ratio, where

$$ {}^{h}/_{\lambda_t} = {}^{h}/_{(\lambda_m \times 0.94)} \, . \tag{3}$$

For the AMB ripples, this correction shifts the measured aspect ratio range from 0.1 – 0.17 (mean = 0.13) to a maximum corrected aspect ratio range of 0.106 – 0.18 (mean = 0.14) which is still consistent with orbital ripples. For the Prow, this correction shifts the measured aspect ratio range from 0.06 – 0.09 (mean = 0.074) to a maximum corrected aspect ratio range of 0.064 – 0.095 (mean = 0.078) which is still lower than typical for orbital ripples but falls within the transition zone where suborbital ripples can form.

The ratio of wavelength to median grain size (λ/D_{50}) can be used to characterize orbital versus anorbital ripples. Anorbital ripples consistently have a λ/D_{50} ratio that falls within the range of 400 – 600, while orbital ripples can have a much larger range of λ/D_{50} (~100 – 2000, inclusive of 400 – 600; *35*). The wavelength to grain size ratio can indicate that ripples are *not* anorbital, if it falls outside the anorbital range, but within that range ripples can be either anorbital or orbital. We used the average measured wavelength for each the AMB and Prow ripple populations to calculate the wavelength-grain size ratio. In the AMB, because grain size is not detectable, we applied the range of possible grain sizes (60 – 180 µm) to estimate a λ/D_{50} range of 750 – 250. This range is non-diagnostic and could correspond to either anorbital ripples (at the smaller end of the possible grain size range) or orbital ripples (throughout the possible grain size range. In the Prow, we used the median grain size calculated from point counts, along with the mean measured wavelength, to calculate a λ/D_{50} value of 118. This ratio is inconsistent with anorbital ripple formation. Substituting the corrected mean λ_t for both the AMB and Prow does not significantly change the wavelength-grain size ratio values for either ripple population.

S3. Wave Ripple Modeling

The wave ripple paleohydraulic reconstructions follow previous work (*54, 56*), and codes are available in supplementary material from (*56*). We calculated the significant wave heights, *H*, and wave periods, *T*, for a given wind fetch, *F*, wind speed, U_w, and water depth, *h*, using a semi-empirical wave forecasting model applicable for shallow and deep water (*42*),

$$H = \frac{{U_A}^2}{g}\ 0.283 \tanh\left(0.53\ \mathrm{h}_s{}^{0.75}\right) tanh\left(\frac{0.00565 F_s^{1/2}}{\tanh(0.53 \mathrm{h}_s{}^{0.75})}\right) \quad (4)$$

$$T = \frac{U_A}{g}\ 7.54 \tanh\left(0.833\ \mathrm{h}_s{}^{3/8}\right) tanh\left(\frac{0.0379 F_s^{0.33}}{\tanh(0.833 \mathrm{h}_s{}^{3/8})}\right) \quad (5)$$

in which $F_s = \frac{gF}{U_A^2}$ is the dimensionless fetch, $h_s = \frac{gh}{U_A^2}$ is the dimensionless water depth, U_A is a wind stress factor (units m/s), g is the acceleration of gravity. The model explicitly incorporates gravity through dimensional analysis due to the important role that gravity plays as the restoring force in wind wave (i.e., surface gravity wave) kinematics.

The model uses a wind stress factor (also called an adjusted wind speed factor), rather than wind speed directly, because as water waves evolve, they change the roughness at the water-air interface which influences the boundary stress for a given wind speed. Wind drag becomes increasingly large at fast wind speeds due to boundary roughness created by surface gravity waves. Coastal Engineering Research Center (*55*) used an empirical relation to relate wind speed, U_w, measured at 10 m elevation above the water surface, to the wind stress factor, U_A, where both velocities are given in m/s,

$$U_A = 0.71{U_w}^{1.23} \quad (6)$$

Equation (6) is applicable to terrestrial conditions, but it requires modification for Mars because it does not explicitly include a term for atmospheric density, ρ, which should strongly influence the boundary stress for a given wind speed. Eq. (6) also does not explicitly include gravity, which affects wave heights (as shown in Eq. 4), and therefore would influence drag at the boundary.

To adapt Eq. (6) to martian conditions, we developed an alternate version that allows the wind speed to be converted into a wind stress factor with explicit consideration of gravity and atmospheric density by following turbulent boundary layer theory. Our derivation follows a scaling relation for the log-law for turbulent boundary layers (*64*), in which wind speed at elevation *z* is

$$U_w \propto \sqrt{\frac{\tau}{\rho}}\left(\frac{z}{k_s}\right)^n \tag{7}$$

where τ is the boundary shear stress, k_s is the boundary roughness height and *n* is a constant that approximates the natural logarithm. For the case of wind generated waves, k_s is set by the wave height, which in turn scales with ${U_A}^2/g$ (Eq. 4) or equivalently $(\frac{\tau}{\rho})/g$ because $\tau \propto \rho {U_A}^2$. Therefore, we set $k_s \propto (\frac{\tau}{\rho})/g$ in Eq. (7), which yields

$$U_w \propto \left(\frac{\tau}{\rho}\right)^{0.5-n} (zg)^n \tag{8}$$

where *n* was found to be *n* = 0.0935 to match the dependencies in Eq (6) for terrestrial conditions. To find the wind speeds on Mars, or any planet, that produce the equivalent stresses on the water surface as on Earth, we took Eq. (8), rearranged it as an expression for τ, specified a generic scenario (subscript *m*) and an Earth scenario (subscript *e*) and set τ equal between the two scenario resulting in

$$U_{wm} = U_{we}\left(\frac{\rho_e}{\rho_m}\right)^{0.5-n}\left(\frac{g_m}{g_e}\right)^n \tag{9}$$

in which we assumed any constants in Eq. (8) (e.g., von Kármán's constant) are indeed constants, and therefore cancel out in Eq. (9), and the height above the water surface, *z*, is the same under both scenarios (i.e., *z* = 10 m). Setting U_w=U_{we} in Eq. (6) and combining it with Eq. (9) results in a prediction of the wind stress factor for any values of atmospheric density and gravity that is mathematically equivalent to Eq. (6) for terrestrial conditions,

$$U_A = 0.71{U_{wm}}^{1.23}\sqrt{\frac{\rho_m}{\rho_e}}\left(\frac{g_m}{g_e}\right)^{-0.115} \tag{10}$$

We used Eq. (10) in place of Eq. (6) in the wave forecasting model (Eqs. 4 and 5). In preliminary tests, we found that the relatively simple wave forecasting model we used provided quantitatively similar results to the SWAN wave model implemented in Delft-3D modeling suite that was adjusted for martian conditions (*11*).

With wave height and wave period calculated from the wave forecasting model, we used Airy wave theory for intermediate-depth waves to find the near-bed wave orbital diameter, d_o, and the wave orbital velocity, U_o. By Airy wave theory,

$$d_o = H/\sinh(\frac{2\pi h}{L}) \tag{11}$$

$$U_o = \frac{\pi d_o}{T} \tag{12}$$

in which L is the wavelength of the wave given by

$$L = \frac{gT^2}{2\pi}\, tanh\left(\frac{2\pi h}{L}\right). \tag{13}$$

We used an iterative scheme to solve Eq. (11-13), and we did not report a solution where waves were expected to break, which violates Airy wave theory. The breaking criteria is (e.g., *65*)

$$H > 0.142\ \frac{2\pi L^2}{gT^2} \tag{14}$$

Airy wave theory is a linear theory for the motion of gravity waves that can be derived from first principles and therefore the dependencies on gravity are known. The theory assumes potential flow (inviscid and irrotational) and, despite its simplicity, compares well to observations of waves in oceans and lakes. Non-linear wave theories are also well established, but the improvement they offer is minimal in comparison to other uncertainties inherent in a paleo-environmental reconstruction of this type.

To predict the wavelength of orbital wave ripples, we used $\lambda = 0.65 d_o$ (e.g., *66*). In addition to creating waves with the appropriate wave orbital diameter, the near bed oscillations must be of sufficient strength to move sand and produce ripples. The grey shaded zone in Fig. 4 shows the range in which ripples are expected to develop based on sediment transport constraints (*57*), where we assumed a median grain diameter of D_{50} = 100 µm (for the AMB ripples), density of sediment of $\rho_s = 3000$ kg/m^3, consistent with a mafic lithology, and water density of ρ_w =1000 kg/m^3. The criteria of (*57*) uses a dimensionless particle diameter,

$$s_* = (RgD)^{0.5} D/(4\nu) \tag{15}$$

where $\nu = 10^{-6}$ m^2/s is the kinematic viscosity of water, and $R = (\rho_s - \rho_w)/\rho_w$. They found that the wave orbital velocity that corresponds to the onset of different bedform regimes is

$$U_o = 2\pi C\left[1 + 5(\frac{3T_0}{T})^2\right]^{-1/4} \tag{16}$$

in which C and T_0 are empirical variables that vary for different bed states. For the onset of ripples, You and Yin (*41*) found that $C = 5.5\left(\frac{\nu}{D}\right) {s_*}^{0.78}$ and $T_0 = 169\frac{D^2}{\nu}{s_*}^{-1.64}$. We set the upper bound on ripples to their sheet flow regime given by $C = 13.5(\frac{\nu}{D}){s_*}^{0.78}$ and $T_0 = 30\frac{D^2}{\nu}{s_*}^{-1.3}$, beyond which hummocks or plane bed is likely to form.

Figure 4 shows the results of wave conditions that can produce wave ripples at the observed ripple wavelengths plotted as a function of water depth, h, and wind speed, U_{wm}, at 10 m above the water surface with a fetch of F = 500 m, and with ρ_m set to either modern martian (ρ_m= 0.02 kg/m^3) or terrestrial (ρ_e = 1.2 kg/m^3) conditions, using martian gravity g_m=3.71 m/s^2 for both scenarios. Figure S6 shows the same model results but with F = 5 km (Fig. S6A) and F = 200 m (Fig. S6B). We performed the calculation through iteration. We first guessed the wind speed, U_{wm}, and calculated the wind stress factor, U_A, from Eq. (10). Next we guessed the water depth and found the wave height and wave period for a given fetch from Eqs. (4) and (5). We input those results into Eq. (11)-(14) to find the corresponding orbital diameter and ripple wavelength. We reported solutions for water depth and wind speed where the calculated ripple wavelength matched the observed wavelength.

S4. Consideration of gravity on Mars

Gravity is an important force in several of the processes considered in this study. In some cases, gravity dependent relations are well established from classical mechanics or through dimensional analysis where the important forces are well known. In our study, these cases include the physics of waves at the water surface driven by wind, where the restoring force is gravity (surface gravity waves). The role of gravity in determining orbital motions below wind waves are known according to Airy wave theory, and the acceleration of gravity is explicit (Eq. 11-14). The theory for wind wave height and period as a function of fetch and wind speed (Eqs. 4, 5) are semi-empirical. Nonetheless, the dependencies on gravity in the relations are likely robust as they are required for dimensional similarity. As discussed above, we derived a more mechanistic version of the wind stress factor (Eq. 10) that explicitly includes gravity and air density based on turbulent boundary layer theory.

Dimensional analysis also is used in sediment transport and bedform theory (*67*, *68*) where gravity affects sediment mobility and settling. While sediment transport can be complex, the primary influence of gravity is through the buoyant weight of sediment. The buoyant weight of course has a well-known dependency on gravity through Archimedes' principle and is known exactly. The criterion we used for the stability of ripples includes this most important effect through RgD in Eq. (15). While directly testing the gravity dependencies in these models is difficult, it is reassuring that for over 100 years, engineers have used similar semi-empirical theories to formulate robust models for hydraulics and sediment transport that can be applied across laboratory scales to natural field scales (*69*). Likewise dimensional analysis has proven successful in predicting bedform dimensions across particles and fluids with different densities and different fluid viscosities (e.g., *38*, *68*, *70*).

There is less known about the role of gravity in the ripple shape indices that we used to classify ripples. Because these relations are geometric, they do not explicitly consider gravity. Here we offer some speculation. The symmetry index of a ripple was used to determine wave ripples from current ripples. Owing to unidirectional flow, current ripples develop a highly asymmetric shape, whereas the oscillatory near-bed motions under waves develop symmetrical ripples (*71*). Orbital ripples have wavelengths that are about two-thirds the near-bed orbital diameter of the fluid motion at equilibrium as a result of resonance between the vortical flow structure and the bed (*72*). They also tend to have a consistent aspect ratio, h/λ, set by the vortex separation zone that forms on the ripple flanks and the angle of repose of the sediment (*72*). These wave ripple scaling relations are only weakly dependent on the vigor of sediment transport (e.g., *66*). Thus, we do not expect them to differ with gravity.

The physics are less clear for the classification of orbital and anorbital wave ripples based on λ/D_{50}. Anorbital ripples can form at high stages of sediment transport (large shear stresses relative to the particle weight) when conditions approach upper plane bed, or during large period oscillations where ripple migration direction switches direction with each oscillation (*73*). Thus, the transition might depend on the vigor of sediment transport, in which case the buoyant weight of sediment could be needed. Dimensional analysis indicates that the wavelength of unidirectional current ripples scales weakly (to the 1/6 power) with gravity (*38*). It is unknown why anorbital ripples are associated with a certain range of λ/D_{50} or whether that range is gravity dependent. Direct numerical simulations could be used to investigate this problem under reduced gravity.

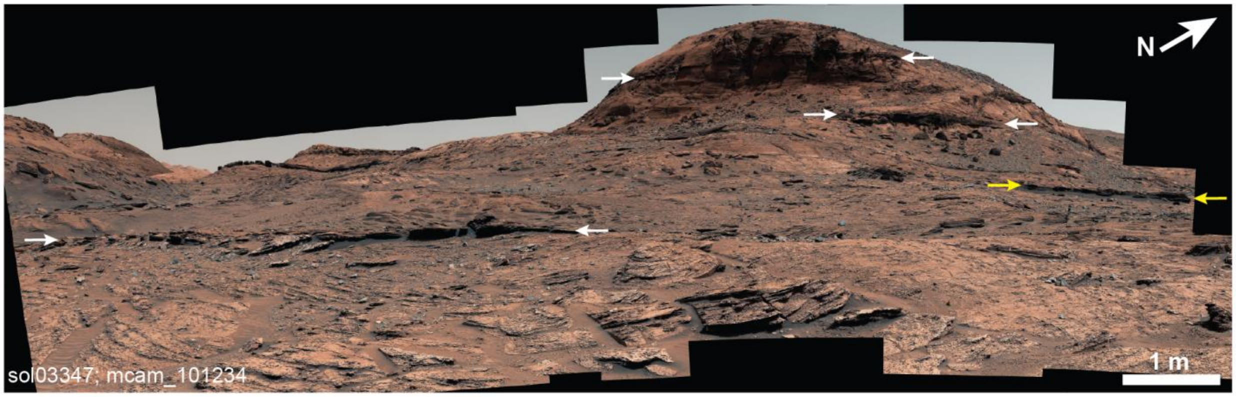

fig. S1. The Prow and other dark-toned lenses

Uncropped, high-resolution image of the Prow outcrop (in between yellow arrows) and other dark-toned, lenticular outcrops (white arrows) around the base of Mirador butte within the predominantly aeolian Mirador formation. Scale bar is accurate to foreground. Image credit: NASA/JPL-Caltech/MSSS

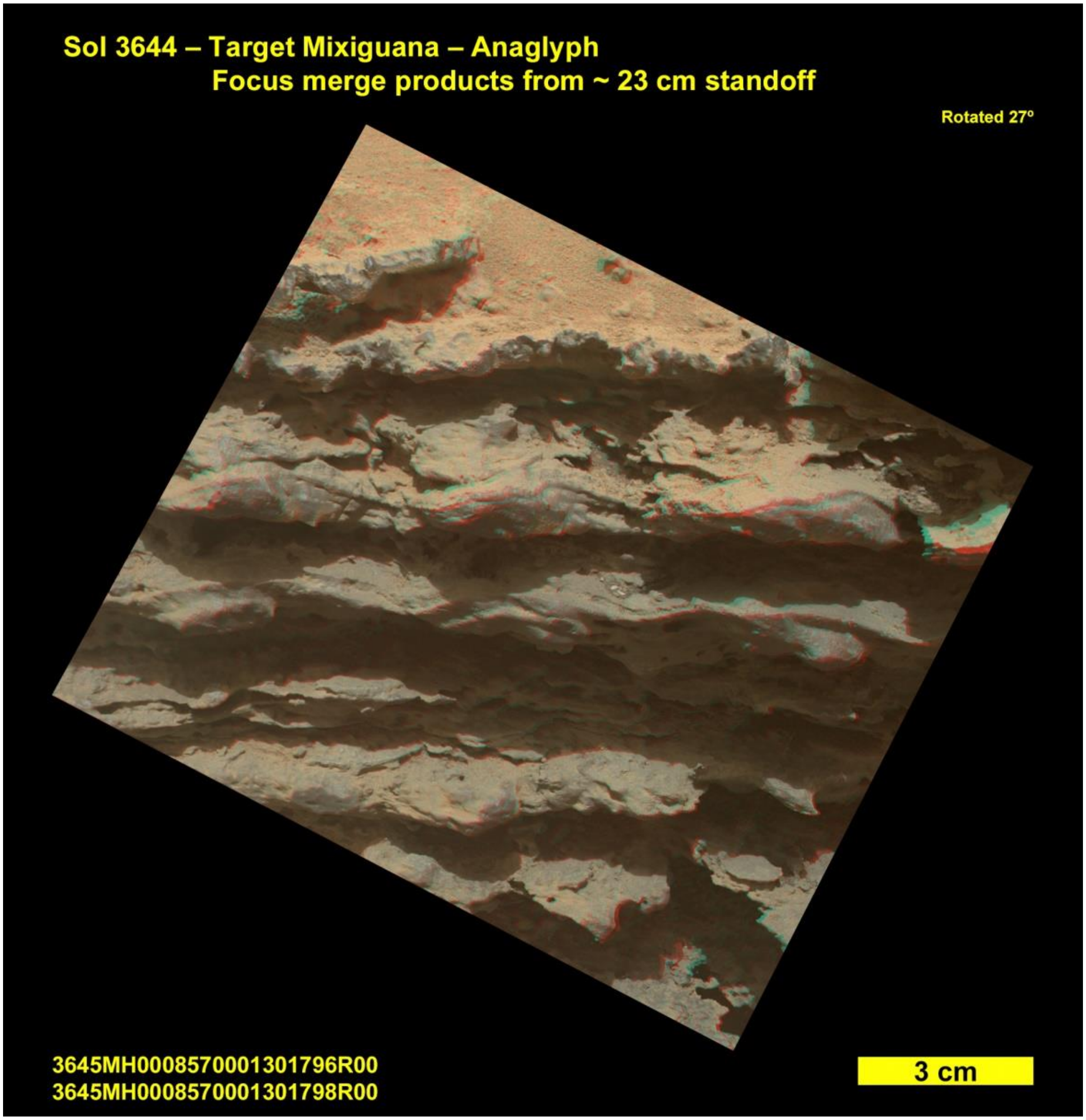

fig. S2. 3D anaglyph of Amapari ripples

Mars Hand Lens Imager (MAHLI) anaglyph image of the ripples in the Amapari Marker Band at the Amapari location. Red/blue 3D glasses required. Image credit: NASA/JPL-Caltech/MSSS

fig. S3. Example of additional Amapari ripples

Cropped image showing another view of ripples in the Amapari Marker Band. Beneath the uppermost resistant ripple layer, laminae within the recessive layer can be seen draping across the underlying ripple crests. Image credit: NASA/JPL-Caltech/MSSS

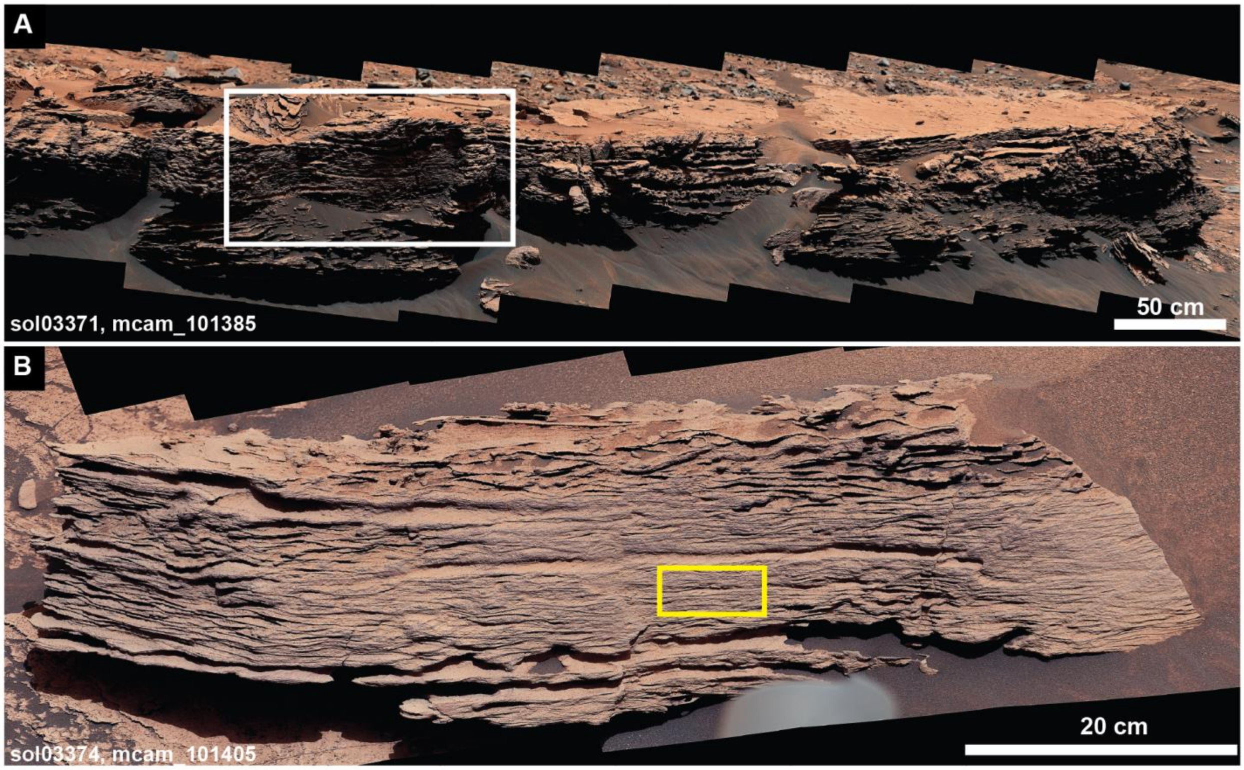

fig. S4. Location of Prow grain size image

Images showing the location of the MAHLI image from Fig. 3E. The MAHLI image (B; yellow square) was acquired on a float block from the middle of the Prow outcrop (A: white square).

(A) Mastcam mosaic: sol03371, mcam_101385, the prow context 23x2L0R0, cropped.

(B) Mastcam mosaic: sol03374, mcam_101405, toron stereo 7x2 L0R0, cropped.

Image credit: NASA/JPL-Caltech/MSSS

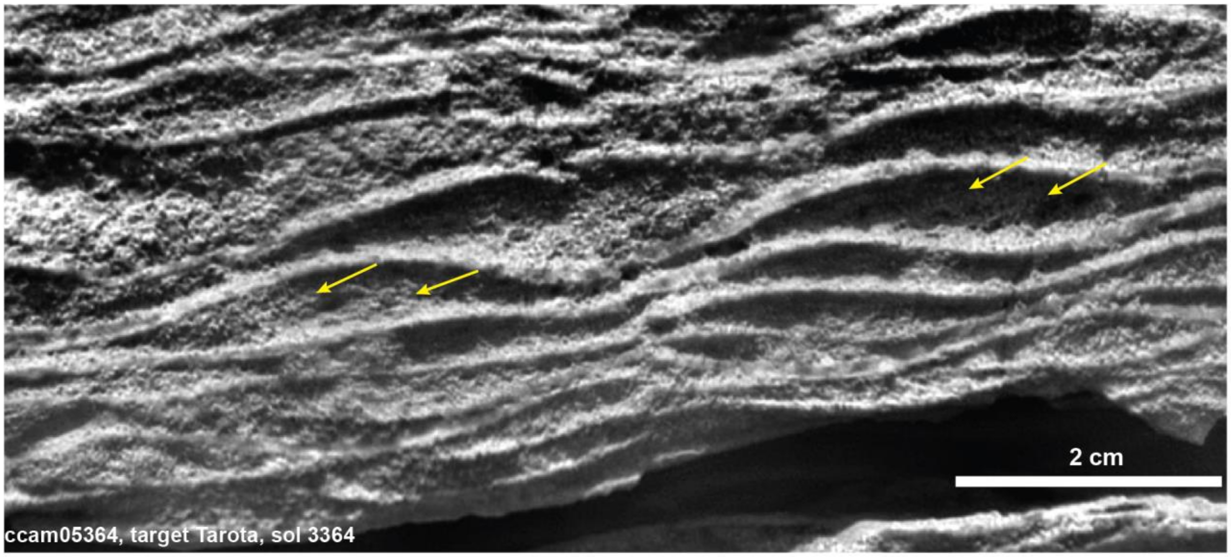

fig. S5. Possible lateral accretion within Prow ripples

Close-up of symmetric ripple in Prow outcrop showing laminae within the ripple forming a possible pattern of lateral accretion to the left (yellow arrows). Zoomed view of right ripples shown in Fig 3C. Image credit: NASA/JPL-Caltech

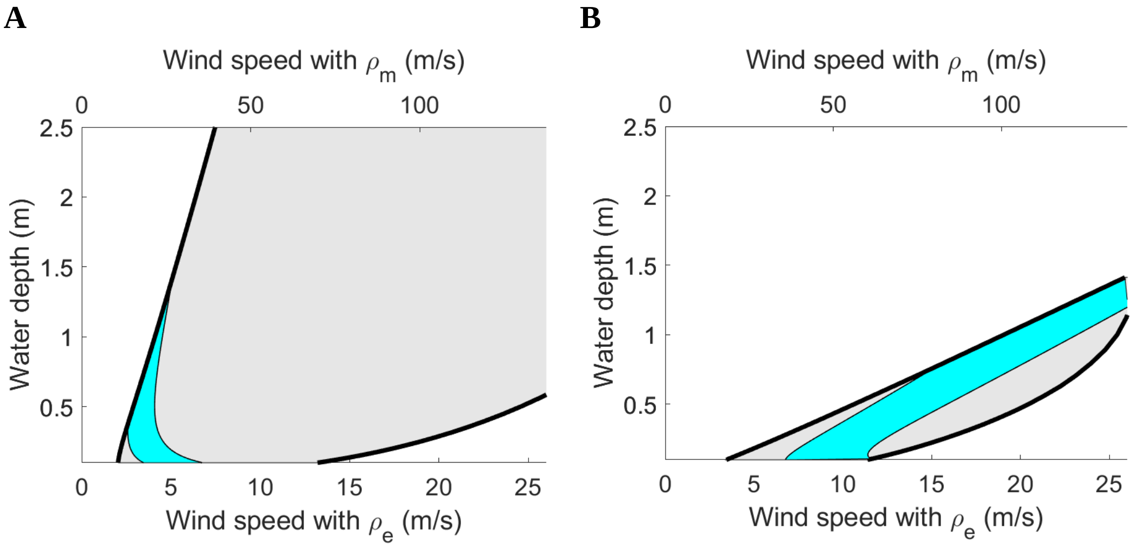

fig. S6. Modeled water depth and wind speed of AMB ripples under different fetch

Conditions to produce orbital wave ripples with 3-6 cm wavelength are shown in the blue shaded zone for 100 μm sand. Ripples of any wavelength form in the gray shaded zone, which is bounded by the thresholds to move sand and generate ripples on one side and the threshold for wave breaking on the other side. For all calculations shown here, wave breaking rather than upper plane bed is the limiting factor for the higher energy range of ripple formation. The calculations are identical to Figure 4 except for single parameter changes. Using the atmospheric densities for modern Mars and Earth, we changed the fetch from 500 m to (**A**) 5 km and (**B**) 200 m. In panel (A) a much larger fetch of 5 km can produce ripples over a wide range of wind speeds, but water depths must be small (< 1.2 m) to limit wave sizes due to bottom friction such that ripples wavelengths are only 3-6 cm. Greater depths would produce larger ripples. Increasing the fetch more does not change the result as the wave sizes are depth limited. In panel (B), a larger wind speed or smaller water depth is required to produce the ripples for the case with a smaller fetch. However, wind speeds greater than about 26 m/s (for ρ_e) result in wave breaking, thus limiting water depths to less than 1.5 m. Reducing the fetch further reduces the water depth range in which ripples form and for fetch < ~100 m, wave breaking occurs for all the needed wave conditions. Hence, we infer that symmetrical wave ripples do not form.

table S1.

Amapari Marker Band (AMB) ripple morphology measurements

Amapari Marker Band						
instrument, image ID, target (sol)	pixel resolution (cm/px)	measured wavelength, λ_m (cm)	height, h (cm)	aspect ratio (h/ λ_m)	outcrop orientation	symmetry index*
MAHLI, mhli00856, Mixiguana (3644)	0.0096	4.34	0.72	0.17	40° *± 10°*	1.07
		4.25	0.58	0.14		0.94
		5.09	0.57	0.11		1.05
		5.13	0.53	0.10		1.08
		4.45	0.47	0.11		0.92
ChemCam LD-RMI, ccam2641, Pintada (3641)	0.0067	4.24	0.66	0.16	40° *± 10°*	1.07
		3.83	0.66	0.17		1.01
		5.01	0.61	0.12		0.76
		3.91	0.51	0.13		1.00
		4.50	0.51	0.11		0.73
ChemCam LD-RMI, ccam3637a, Marker Band (3637)	0.059	5.32	0.71	0.13	25° *± 10°*	0.95
		4.44	0.71	0.16		0.80
		4.26	0.47	0.11		1.15
		4.14	0.59	0.14		1.29
		4.08	0.65	0.16		0.78
		4.32	0.53	0.12		0.82
	minimum	3.83	0.47	0.10		0.73
	average	**4.46**	**0.59**	**0.13**		**0.96**
	maximum	5.32	0.72	0.17		1.29

AMB ripple crest orientation = 315°/135° ± 10°

table S2.

The Prow ripple morphology measurements

The Prow						
instrument, image ID, target (sol)	pixel resolution (cm/px)	measured wavelength, λ_m (cm)	height, h (cm)	aspect ratio (h/ λ_m)	outcrop orientation	symmetry index*
ChemCam LD-RMI, ccam05364, Tarota (sol3364)	0.0074	4.01	0.23	0.057	130° *± 10°*	0.84
		4.50	0.30	0.066		1.12
		4.34	0.39	0.090		1.06
		3.48	0.32	0.091		0.94
		5.48	0.34	0.062		1.10
		3.61	0.23	0.064		1.16
ChemCam LD-RMI, ccam05371, Yuruani (sol 3371)	0.0102	5.09	0.44	0.087	120° *± 10°*	0.78
		5.07	0.40	0.079		1.09
		5.36	0.37	0.070		0.90
		5.86	0.45	0.076		1.00
		4.64	0.34	0.073		1.32
	minimum	3.48	0.23	0.06		0.78
	average	**4.68**	**0.35**	**0.074**		**1.00**
	maximum	5.86	0.45	0.09		1.16

Prow ripple crest orientation = 215°/035° ± 10°

REFERENCES AND NOTES

1. A. G. Fairén, C. R. Stokes, N. S. Davies, D. Schulze-Makuch, J. A. P. Rodríguez, A. F. Davila, E. R. Uceda, J. M. Dohm, V. R. Baker, S. M. Clifford, C. P. McKay, S. W. Squyres, A cold hydrological system in Gale crater, Mars. *Planet. Space Sci.* **93-94**, 101–118 (2014).

2. A. M. Kling, R. M. Haberle, C. P. McKay, T. F. Bristow, F. Rivera-Hernandez, Subsistence of ice-covered lakes during the Hesperian at Gale crater, Mars. *Icarus* **338**, 113495 (2020).

3. R. M. Ramirez, R. A. Craddock, The geological and climatological case for a warmer and wetter early Mars. *Nat. Geosci.* **11**, 230–237 (2018).

4. N. G. Barlow, *Mars: An Introduction to Its Interior, Surface and Atmosphere* (Cambridge Univ. Press, 2009).

5. A. D. Howard, J. M. Moore, R. P. Irwin III, An intense terminal epoch of widespread fluvial activity on early Mars: 1. Valley network incision and associated deposits. *J. Geophys. Res. Planets* **110**, E12S14 (2005).

6. M. C. Malin, K. S. Edgett, Sedimentary rocks of early Mars. *Science* **290**, 1927–1937 (2000).

7. N. Mangold, C. Quantin, V. Ansan, C. Delacourt, P. Allemand, Evidence for precipitation on Mars from dendritic valleys in the Valles Marineris area. *Science* **305**, 78–81 (2004).

8. R. D. Wordsworth, The climate of early Mars. *Annu. Rev. Earth Planet. Sci.* **44**, 381–408 (2016).

9. E. S. Kite, L. J. Steele, M. A. Mischna, M. I. Richardson, Warm early Mars surface enabled by high-altitude water ice clouds. *Proc. Natl. Acad. Sci. U.S.A.* **118**, e2101959118 (2021).

10. R. Wordsworth, A. H. Knoll, J. Hurowitz, M. Baum, B. L. Ehlmann, J. W. Head, K. Steakley, A coupled model of episodic warming, oxidation and geochemical transitions on early Mars. *Nat. Geosci.* **14**, 127–132 (2021).

11. D. M. Rubin, M. A. G. Lapôtre, A. W. Stevens, M. P. Lamb, C. M. Fedo, J. P. Grotzinger, S. Gupta, K. M. Stack, A. R. Vasavada, S. G. Banham, A. B. Bryk, G. Caravaca, J. R. Christian, L.

A. Edgar, M. C. Malin, Ancient winds, waves, and atmosphere in Gale crater, Mars, inferred from sedimentary structures and wave modeling. *J. Geophys. Res. Planets* **127**, e2021JE007162 (2022).

12. J. P. Grotzinger, A. G. Hayes, M. P. Lamb, S. M. McLennan, Sedimentary processes on earth, Mars, titan, and Venus, in *Comparative Climatology of Terrestrial Planets* (University of Arizona Press, 2013), pp. 439–472.

13. S. G. Banham, S. Gupta, D. M. Rubin, J. A. Watkins, D. Y. Sumner, K. S. Edgett, J. P. Grotzinger, K. W. Lewis, L. A. Edgar, K. M. Stack-Morgan, R. Barnes, J. F. Bell, M. D. Day, R. C. Ewing, M. G. A. Lapotre, N. T. Stein, F. Rivera-Hernandez, A. R. Vasavada, Ancient Martian aeolian processes and palaeomorphology reconstructed from the Stimson formation on the lower slope of Aeolis Mons, Gale crater, Mars. *Sedimentology* **65**, 993–1042 (2018).

14. L. A. Edgar, C. M. Fedo, S. Gupta, S. G. Banham, A. A. Fraeman, J. P. Grotzinger, K. M. Stack, N. T. Stein, K. A. Bennett, F. Rivera-Hernández, V. Z. Sun, K. S. Edgett, D. M. Rubin, C. House, J. Van Beek, A lacustrine paleoenvironment recorded at Vera RubinRidge, Gale crater: Overview of the sedimentology and stratigraphy observed by the Mars Science Laboratory Curiosity Rover. *J. Geophys. Res. Planets* **125**, e2019JE006307 (2020).

15. J. P. Grotzinger, R. E. Arvidson, J. F. Bell III, W. Calvin, B. C. Clark, D. A. Fike, M. Golombek, R. Greeley, A. Haldemann, K. E. Herkenhoff, B. L. Jolliff, A. H. Knoll, M. Malin, S. M. McLennan, T. Parker, L. Soderblom, J. N. Sohl-Dickstein, S. W Squyers, N. J. Tosca, W. A. Watters, Stratigraphy and sedimentology of a dry to wet eolian depositional system, Burns formation, Meridiani Planum, Mars. *Earth Planet. Sci. Lett.* **240**, 11–72 (2005).

16. J. P. Grotzinger, D. Y. Sumner, L. C. Kah, K. Stack, S. Gupta, L. Edgar, D. Rubin, K. Lewis, J. Schieber, N. Mangold, R. Milliken, P. G. Conrad, D. Des Marais, J. Farmer, K. Siebach, F. Calef, III, J. Hurowitz, S. M. Mc Lennan, D. Ming, D. Vaniman, J. Crisp, A. Vasavada, K. S. Edgett, M. Malin, D. Blake, R. Gellert, P. Mahaffy, R. C. Wiens, S. Maurice, J. A. Grant, S. Wilson, R. C. Anderson, L. Beegle, R. Arvidson, B. Hallet, R. S. Sletten, M. Rice, J. Bell, III, J. Griffes, B. Ehlmann, R. B. Anderson, T. F. Bristow, W. E. Dietrich, G. Dromart, J. Eigenbrode, A. Fraeman, C. Hardgrove, K. Herkenhoff, L. Jandura, G. Kocurek, S. Lee, L. A. Leshin, R.

Leveille, D. Limonadi, J. Maki, S. Mc Closkey, M. Meyer, M. Minitti, H. Newsom, D. Oehler, A. Okon, M. Palucis, T. Parker, S. Rowland, M. Schmidt, S. Squyres, A. Steele, E. Stolper, R. Summons, A. Treiman, R. Williams, A. Yingst, MSL Science Team, O. Kemppinen, N. Bridges, J. R. Johnson, D. Cremers, A. Godber, M. Wadhwa, D. Wellington, I. M. Ewan, C. Newman, M. Richardson, A. Charpentier, L. Peret, P. King, J. Blank, G. Weigle, S. Li, K. Robertson, V. Sun, M. Baker, C. Edwards, K. Farley, H. Miller, M. Newcombe, C. Pilorget, C. Brunet, V. Hipkin, R. Léveillé, G. Marchand, P. S. Sánchez, L. Favot, G. Cody, L. Flückiger, D. Lees, A. Nefian, M. Martin, M. Gailhanou, F. Westall, G. Israël, C. Agard, J. Baroukh, C. Donny, A. Gaboriaud, P. Guillemot, V. Lafaille, E. Lorigny, A. Paillet, R. Pérez, M. Saccoccio, C. Yana, C. Armiens-Aparicio, J. C. Rodríguez, I. C. Blázquez, F. G. Gómez, J. Gómez-Elvira, S. Hettrich, A. L. Malvitte, M. M. Jiménez, J. Martínez-Frías, J. Martín-Soler, F. J. Martín-Torres, A. M. Jurado, L. Mora-Sotomayor, G. M. Caro, S. N. López, V. Peinado-González, J. Pla-García, J. A. R. Manfredi, J. J. Romeral-Planelló, S. A. S. Fuentes, E. S. Martinez, J. T. Redondo, Roser Urqui-O'Callaghan, M.-P. Z. Mier, S. Chipera, J.-L. Lacour, P. Mauchien, J.-B. Sirven, H. Manning, A. Fairén, A. Hayes, J. Joseph, R. Sullivan, P. Thomas, A. Dupont, A. Lundberg, N. Melikechi, A. Mezzacappa, J. De Marines, D. Grinspoon, G. Reitz, B. Prats, E. Atlaskin, M. Genzer, A.-M. Harri, H. Haukka, H. Kahanpää, J. Kauhanen, M. Paton, J. Polkko, W. Schmidt, T. Siili, C. Fabre, J. Wray, M. B. Wilhelm, F. Poitrasson, K. Patel, S. Gorevan, S. Indyk, G. Paulsen, D. Bish, B. Gondet, Y. Langevin, C. Geffroy, D. Baratoux, G. Berger, A. Cros, C. d'Uston, O. Forni, O. Gasnault, J. Lasue, Q.-M. Lee, P.-Y. Meslin, E. Pallier, Y. Parot, P. Pinet, S. Schröder, M. Toplis, É. Lewin, W. Brunner, E. Heydari, C. Achilles, B. Sutter, M. Cabane, D. Coscia, C. Szopa, F. Robert, V. Sautter, S. L. Mouélic, M. Nachon, A. Buch, F. Stalport, P. Coll, P. François, F. Raulin, S. Teinturier, J. Cameron, S. Clegg, A. Cousin, D. De Lapp, R. Dingler, R. S. Jackson, S. Johnstone, N. Lanza, C. Little, T. Nelson, R. B. Williams, A. Jones, L. Kirkland, B. Baker, B. Cantor, M. Caplinger, S. Davis, B. Duston, D. Fay, D. Harker, P. Herrera, E. Jensen, M. R. Kennedy, G. Krezoski, D. Krysak, L. Lipkaman, E. M. Cartney, S. M. Nair, B. Nixon, L. Posiolova, M. Ravine, A. Salamon, L. Saper, K. Stoiber, K. Supulver, J. Van Beek, T. Van Beek, R. Zimdar, K. L. French, K. Iagnemma, K. Miller, F. Goesmann, W. Goetz, S. Hviid, M. Johnson, M. Lefavor, E. Lyness, E. Breves, M. D. Dyar, C. Fassett, L. Edwards, R. Haberle, T. Hoehler, J. Hollingsworth, M. Kahre, L. Keely, C. M. Kay, L. Bleacher, W. Brinckerhoff, D. Choi, J. P. Dworkin, M. Floyd, C. Freissinet, J. Garvin, D. Glavin, D. Harpold, D. K. Martin, A.

M. Adam, A. Pavlov, E. Raaen, M. D. Smith, J. Stern, F. Tan, M. Trainer, A. Posner, M. Voytek, A. Aubrey, A. Behar, D. Blaney, D. Brinza, L. Christensen, L. De Flores, J. Feldman, S. Feldman, G. Flesch, I. Jun, D. Keymeulen, M. Mischna, J. M. Morookian, B. Pavri, M. Schoppers, A. Sengstacken, J. J. Simmonds, N. Spanovich, M. de la Torre Juarez, C. R. Webster, A. Yen, P. D. Archer, F. Cucinotta, J. H. Jones, R. V. Morris, P. Niles, E. Rampe, T. Nolan, M. Fisk, L. Radziemski, B. Barraclough, S. Bender, D. Berman, E. N. Dobrea, R. Tokar, T. Cleghorn, W. Huntress, G. Manhès, J. Hudgins, T. Olson, N. Stewart, P. Sarrazin, E. Vicenzi, M. Bullock, B. Ehresmann, V. Hamilton, D. Hassler, J. Peterson, S. Rafkin, C. Zeitlin, F. Fedosov, D. Golovin, N. Karpushkina, A. Kozyrev, M. Litvak, A. Malakhov, I. Mitrofanov, M. Mokrousov, S. Nikiforov, V. Prokhorov, A. Sanin, V. Tretyakov, A. Varenikov, A. Vostrukhin, R. Kuzmin, B. Clark, M. Wolff, O. Botta, D. Drake, K. Bean, M. Lemmon, S. P. Schwenzer, E. M. Lee, R. Sucharski, M. Á. de Pablo Hernández, J. J. B. Ávalos, M. Ramos, M.-H. Kim, C. Malespin, I. Plante, J.-P. Muller, R. Navarro-González, R. Ewing, W. Boynton, R. Downs, M. Fitzgibbon, K. Harshman, S. Morrison, O. Kortmann, A. Williams, G. Lugmair, M. A. Wilson, B. Jakosky, T. Balic-Zunic, J. Frydenvang, J. K. Jensen, K. Kinch, A. Koefoed, M. B. Madsen, S. L. S. Stipp, N. Boyd, J. L. Campbell, G. Perrett, I. Pradler, S. Van Bommel, S. Jacob, T. Owen, H. Savijärvi, E. Boehm, S. Böttcher, S. Burmeister, J. Guo, J. Köhler, C. M. García, R. Mueller-Mellin, R. Wimmer-Schweingruber, J. C. Bridges, T. M. Connochie, M. Benna, H. Franz, H. Bower, A. Brunner, H. Blau, T. Boucher, M. Carmosino, S. Atreya, H. Elliott, D. Halleaux, N. Rennó, M. Wong, R. Pepin, B. Elliott, J. Spray, L. Thompson, S. Gordon, A. Ollila, J. Williams, P. Vasconcelos, J. Bentz, K. Nealson, R. Popa, J. Moersch, C. Tate, M. Day, R. Francis, E. M. Cullough, E. Cloutis, I. L. ten Kate, D. Scholes, S. Slavney, T. Stein, J. Ward, J. Berger, J. E. Moores, A habitable fluvio-lacustrine environment at Yellowknife Bay, Gale Crater, Mars. *Science* **343**, 1242777 (2014).

17. K. M. Stack, J. P. Grotzinger, M. P. Lamb, S. Gupta, D. M. Rubin, L. C. Kah, L. A. Edgar, D. M. Fey, J. A. Hurowitz, M. M. Bride, F. Rivera-Hernández, D. Y. Sumner, J. K. Van Beek, R. M. E. Williams, R. A. Yingst, Evidence for plunging river plume deposits in the Pahrump Hills member of the Murray formation, Gale crater, Mars. *Sedimentology* **66**, 1768–1802 (2019).

18. R. M. E. Williams, J. P. Grotzinger, W. E. Dietrich, S. Gupta, D. Y. Sumner, R. C. Wiens, N. Mangold, M. C. Malin, K. S. Edgett, S. Maurice, O. Forni, O. Gasnault, A. Ollila, H. E.

Newsom, G. Dromart, M. C. Palucis, R. A. Yingst, R. B. Anderson, K. E. Herkenhoff, S. Le Mouélic, W. Goetz, M. B. Madsen, A. Koefoed, J. K. Jensen, J. C. Bridges, S. P. Schwenzer, K. W. Lewis, K. M. Stack, D. Rubin, L. C. Kah, J. F. Bell, III, J. D. Farmer, R. Sullivan, T. Van Beek, D. L. Blaney, O. Pariser, R. G. Deen, MSL Science Team, O. Kemppinen, N. Bridges, J. R. Johnson, M. Minitti, D. Cremers, L. Edgar, A. Godber, M. Wadhwa, D. Wellington, I. M. Ewan, C. Newman, M. Richardson, A. Charpentier, L. Peret, P. King, J. Blank, G. Weigle, M. Schmidt, S. Li, R. Milliken, K. Robertson, V. Sun, M. Baker, C. Edwards, B. Ehlmann, K. Farley, J. Griffes, H. Miller, M. Newcombe, C. Pilorget, M. Rice, K. Siebach, E. Stolper, C. Brunet, V. Hipkin, R. Léveillé, G. Marchand, P. S. Sánchez, L. Favot, G. Cody, A. Steele, L. Flückiger, D. Lees, A. Nefian, M. Martin, M. Gailhanou, F. Westall, G. Israël, C. Agard, J. Baroukh, C. Donny, A. Gaboriaud, P. Guillemot, V. Lafaille, E. Lorigny, A. Paillet, R. Pérez, M. Saccoccio, C. Yana, C. A. Aparicio, J. C. Rodríguez, I. C. Blázquez, F. G. Gómez, J. G. Elvira, S. Hettrich, A. L. Malvitte, M. M. Jiménez, J. M. Frías, J. M. Soler, F. J. M. Torres, A. M. Jurado, L. M. Sotomayor, G. M. Caro, S. N. López, V. P. González, J. P. García, J. A. Rodriguez Manfredi, J. J. Romeral Planelló, S. A. Sans Fuentes, E. S. Martinez, J. T. Redondo, R. U. O’Callaghan, M.-P. Zorzano Mier, S. Chipera, J.-L. Lacour, P. Mauchien, J.-B. Sirven, H. Manning, A. Fairén, A. Hayes, J. Joseph, S. Squyres, P. Thomas, A. Dupont, A. Lundberg, N. Melikechi, A. Mezzacappa, J. De Marines, D. Grinspoon, G. Reitz, B. Prats, E. Atlaskin, M. Genzer, A.-M. Harri, H. Haukka, H. Kahanpää, J. Kauhanen, M. Paton, J. Polkko, W. Schmidt, T. Siili, C. Fabre, J. Wray, M. B. Wilhelm, F. Poitrasson, K. Patel, S. Gorevan, S. Indyk, G. Paulsen, D. Bish, J. Schieber, B. Gondet, Y. Langevin, C. Geffroy, D. Baratoux, G. Berger, A. Cros, C. D. Uston, J. Lasue, Q.-M. Lee, P.-Y. Meslin, E. Pallier, Y. Parot, P. Pinet, S. Schröder, M. Toplis, É. Lewin, W. Brunner, E. Heydari, C. Achilles, D. Oehler, B. Sutter, M. Cabane, D. Coscia, C. Szopa, F. Robert, V. Sautter, M. Nachon, A. Buch, F. Stalport, P. Coll, P. François, F. Raulin, S. Teinturier, J. Cameron, S. Clegg, A. Cousin, D. De Lapp, R. Dingler, R. S. Jackson, S. Johnstone, N. Lanza, C. Little, T. Nelson, R. B. Williams, A. Jones, L. Kirkland, A. Treiman, B. Baker, B. Cantor, M. Caplinger, S. Davis, B. Duston, D. Fay, C. Hardgrove, D. Harker, P. Herrera, E. Jensen, M. R. Kennedy, G. Krezoski, D. Krysak, L. Lipkaman, E. M. Cartney, S. M. Nair, B. Nixon, L. Posiolova, M. Ravine, A. Salamon, L. Saper, K. Stoiber, K. Supulver, J. Van Beek, R. Zimdar, K. L. French, K. Iagnemma, K. Miller, R. Summons, F. Goesmann, S. Hviid, M. Johnson, M. Lefavor, E. Lyness, E. Breves, M. D. Dyar, C. Fassett, D. F. Blake, T. Bristow,

D. D. Marais, L. Edwards, R. Haberle, T. Hoehler, J. Hollingsworth, M. Kahre, L. Keely, C. M. Kay, L. Bleacher, W. Brinckerhoff, D. Choi, P. Conrad, J. P. Dworkin, J. Eigenbrode, M. Floyd, C. Freissinet, J. Garvin, D. Glavin, D. Harpold, P. Mahaffy, D. K. Martin, A. M. Adam, A. Pavlov, E. Raaen, M. D. Smith, J. Stern, F. Tan, M. Trainer, M. Meyer, A. Posner, M. Voytek, R. C. Anderson, A. Aubrey, L. W. Beegle, A. Behar, D. Brinza, F. Calef, L. Christensen, J. A. Crisp, L. De Flores, J. Feldman, S. Feldman, G. Flesch, J. Hurowitz, I. Jun, D. Keymeulen, J. Maki, M. Mischna, J. M. Morookian, T. Parker, B. Pavri, M. Schoppers, A. Sengstacken, J. J. Simmonds, N. Spanovich, M. de la Torre Juarez, A. R. Vasavada, C. R. Webster, A. Yen, P. D. Archer, F. Cucinotta, J. H. Jones, D. Ming, R. V. Morris, P. Niles, E. Rampe, T. Nolan, M. Fisk, L. Radziemski, B. Barraclough, S. Bender, D. Berman, E. N. Dobrea, R. Tokar, D. Vaniman, L. Leshin, T. Cleghorn, W. Huntress, G. Manhès, J. Hudgins, T. Olson, N. Stewart, P. Sarrazin, J. Grant, E. Vicenzi, S. A. Wilson, M. Bullock, B. Ehresmann, V. Hamilton, D. Hassler, J. Peterson, S. Rafkin, C. Zeitlin, F. Fedosov, D. Golovin, N. Karpushkina, A. Kozyrev, M. Litvak, A. Malakhov, I. Mitrofanov, M. Mokrousov, S. Nikiforov, V. Prokhorov, A. Sanin, V. Tretyakov, A. Varenikov, A. Vostrukhin, R. Kuzmin, B. Clark, M. Wolff, S. M. Lennan, O. Botta, D. Drake, K. Bean, M. Lemmon, E. M. Lee, R. Sucharski, M. Á. de Pablo Hernández, J. J. B. Ávalos, M. Ramos, M.-H. Kim, C. Malespin, I. Plante, J.-P. Muller, R. N. González, R. Ewing, W. Boynton, R. Downs, M. Fitzgibbon, K. Harshman, S. Morrison, O. Kortmann, A. Williams, G. Lugmair, M. A. Wilson, B. Jakosky, T. B. Zunic, J. Frydenvang, K. Kinch, S. L. S. Stipp, N. Boyd, J. L. Campbell, R. Gellert, G. Perrett, I. Pradler, S. Van Bommel, S. Jacob, T. Owen, S. Rowland, H. Savijärvi, E. Boehm, S. Böttcher, S. Burmeister, J. Guo, J. Köhler, C. M. García, R. M. Mellin, R. W. Schweingruber, T. M. Connochie, M. Benna, H. Franz, H. Bower, A. Brunner, H. Blau, T. Boucher, M. Carmosino, S. Atreya, H. Elliott, D. Halleaux, N. Rennó, M. Wong, R. Pepin, B. Elliott, J. Spray, L. Thompson, S. Gordon, J. Williams, P. Vasconcelos, J. Bentz, K. Nealson, R. Popa, J. Moersch, C. Tate, M. Day, G. Kocurek, B. Hallet, R. Sletten, R. Francis, E. M. Cullough, E. Cloutis, I. L. ten Kate, R. Arvidson, A. Fraeman, D. Scholes, S. Slavney, T. Stein, J. Ward, J. Berger, J. E. Moores, Martian fluvial conglomerates at Gale crater. *Science* **340**, 1068–1072 (2013).

19. L. Edgar, J. Grotzinger, C. M. Fedo, M. Meyer, W. Rapin, W. E. Dietrich, A. B. Bryk, S. Gupta, A. L. Roberts, S. G. Banham, J. Reahl, Wet to dry depositional environments recorded in the

clay-sulfate transition region in Gale crater, Mars: Overview and stratigraphic context for Curiosity's exploration campaign, in *55th Lunar and Planetary Science Conference* (Lunar and Planetary Institute, 2024), p. 1016.

20. S. W. Squyres, J. F. Kasting, Early Mars: How warm and how wet?. *Science* **265**, 744–749 (1994).

21. C. P. McKay, D. T. Andersen, W. H. Pollard, J. L. Heldmann, P. T. Doran, C. H. Fritsen, J. C. Priscu, 9 Polar lakes, streams, and springs as analogs for the hydrological cycle on Mars, in *Water on Mars and Life* (Springer, 2005), pp. 219–233.

22. E. S. Kite, Geologic constraints on early Mars climate. *Space Sci. Rev.* **215**, 10 (2019).

23. L. Le Deit, E. Hauber, F. Fueten, M. Pondrelli, A. P. Rossi, R. Jaumann, Sequence of infilling events in Gale Crater, Mars: Results from morphology, stratigraphy, and mineralogy. *J. Geophys. Res. Planets* **118**, 2439–2473 (2013).

24. J. P. Grotzinger, S. Gupta, M. C. Malin, D. M. Rubin, J. Schieber, K. Siebach, D. Y. Sumner, K. M. Stack, A. R. Vasavada, R. E. Arvidson, F. Calef III, L. Edgar, W. F. Fischer, J. A. Grant, J. Griffes, L. C. Kah, M. P. Lamb, K. W. Lewis, N. Mangold, M. E. Minitti, M. Palucis, M. Rice, R. M. E. Williams, R. A. Yingst, D. Blake, D. Blaney, P. Conrad, J. Crisp, W. E. Dietrich, G. Dromart, K. S. Edgett, R. C. Ewing, R. Gellert, J. A. Hurowitz, G. Kocurek, P. Mahaffy, M. J. McBride, S. M. McLennan, M. Mischna, D. Ming, R. Milliken, H. Newsom, D. Oehler, T. J. Parker, D. Vaniman, R. C. Wiens, S. A. Wilson, Deposition, exhumation, and paleoclimate of an ancient lake deposit, Gale crater, Mars. *Science* **350**, aac7575 (2015).

25. C. M. Fedo, A. B. Bryk, L. A. Edgar, K. A. Bennett, V. K. Fox, W. E. Dietrich, S. G. Banham, S. Gupta, K. M. Stack, R. M. E. Williams, J. P. Grotzinger, N. T. Stein, D. M. Rubin, G. Caravaca, R. E. Arvidson, M. N. Hughes, A. A. Fraeman, A. R. Vasavada, J. Schieber, B. Sutter, Geology and stratigraphic correlation of the Murray and Carolyn Shoemaker formations across the Glen Torridon region, Gale crater, Mars. *J. Geophys. Res. Planets* **127**, e2022JE007408 (2022).

26. N. T. Stein, D. P. Quinn, J. P. Grotzinger, C. Fedo, B. L. Ehlmann, K. M. Stack, L. A. Edgar, A. A. Fraeman, R. Deen, Regional structural orientation of the Mount Sharp group revealed by in situ dip measurements and stratigraphic correlations on the Vera Rubin ridge. *J. Geophys. Res. Planets* **125**, e2019JE006298 (2020).

27. S. Gwizd, C. Fedo, J. Grotzinger, S. Banham, F. Rivera-Hernández, K. M. Stack, K. Siebach, M. Thorpe, L. Thompson, C. O'Connell-Cooper, N. Stein, L. Edgar, S. Gupta, D. Rubin, D. Sumner, A. R. Vasavada, Sedimentological and geochemical perspectives on a marginal lake environment recorded in the Hartmann's Valley and Karasburg members of the Murray formation, Gale crater, Mars. *J. Geophys. Res. Planets* **127**, e2022JE007280 (2022).

28. S. Gwizd, C. Fedo, J. Grotzinger, S. Banham, F. Rivera-Hernández, S. Gupta, K. M. Stack, L. A. Edgar, A. R. Vasavada, J. Davis, L. C. Kah, Evolution of a lake margin recorded in the sutton island member of the Murray Formation, Gale Crater, Mars. *J. Geophys. Res. Planets* **129**, e2023JE007919 (2024).

29. J. Schieber, K. M. Bohacs, M. Coleman, D. Bish, M. H. Reed, L. Thompson, W. Rapin, Z. Yawar, Mars is a mirror—Understanding the Pahrump Hills mudstones from a perspective of Earth analogues. *Sedimentology* **69**, 2371–2435 (2022).

30. G. Caravaca, N. Mangold, E. Dehouck, J. Schieber, L. Zaugg, A. B. Bryk, C. M. Fedo, S. L. Mouélic, L. L. Deit, S. G. Banham, S. Gupta, A. Cousin, W. Rapin, O. Gasnault, F. Rivera-Hernández, R. C. Wiens, N. L. Lanza, From lake to river: Documenting an environmental transition across the Jura/Knockfarril Hill members boundary in the Glen Torridon region of Gale crater (Mars). *J. Geophys. Res. Planets* **127**, e2021JE007093 (2022).

31. B. T. Cardenas, J. P. Grotzinger, M. P. Lamb, K. W. Lewis, C. M. Fedo, A. B. Bryk, W. E. Dietrich, N. Stein, M. Turner, G. Caravaca, Barform deposits of the Carolyn Shoemaker formation, Gale crater, Mars. *J. Sediment. Res.* **92**, 1071–1092 (2022).

32. S. Gupta, L. Edgar, R. A. Yingst, A. B. Bryk, G. Caravaca, W. Dietrich, J. Grotzinger, D. Rubin, W. Rapin, S. Banham, A. Roberts, S. Le Mouélic, R. Williams, J. Schieber, N. Mangold, T. Kubacki, O. Gasnault, R. Wiens, A. Fraeman, A. Vasavada, Episodic aqueous conditions

punctuated dominantly aeolian deposition within the layered sulphate-bearing unit, Gale crater (Mars), in *Europlanet Science Congress* (Europlanet Society, 2022), pp. EPSC2022–963.

33. R. E. Milliken, J. P. Grotzinger, B. J. Thomson, Paleoclimate of Mars as captured by the stratigraphic record in Gale Crater. *Geophys. Res. Lett.* **37**, L04201 (2010).

34. C. M. Weitz, K. W. Lewis, J. L. Bishop, B. J. Thomson, R. E. Arvidson, J. A. Grant, K. D. Seelos, I. Ettenborough, Orbital observations of a marker horizon at Gale crater. *J. Geophys. Res. Planets* **127**, e2022JE007211 (2022).

35. P. L. Wiberg, C. K. Harris, Ripple geometry in wave-dominated environments. *J. Geophys. Res. Oceans* **99**, 775–789 (1994).

36. K. S. Edgett, R. A. Yingst, M. A. Ravine, M. A. Caplinger, J. N. Maki, F. T. Ghaemi, J. A. Schaffner, J. F. Bell III, L. J. Edwards, K. E. Herkenhoff, E. Heydari, L. C. Kah, M. T. Lemmon, M. E. Minitti, T. S. Olson, T. J. Parker, S. K. Rowland, J. Schieber, R. J. Sullivan, D. Y. Sumner, P. C. Thomas, E. H. Jensen, J. J. Simmonds, A. J. Sengstacken, R. G. Willson, W. Goetz, Curiosity’s Mars hand lens imager (MAHLI) investigation. *Space Sci. Rev.* **170**, 259–317 (2012).

37. J. F. M. De Raaf, J. R. Boersma, S. Van Gelder, Wave-generated structures and sequences from a shallow marine succession, Lower Carboniferous, County Cork, Ireland. *Sedimentology* **24**, 451–483 (1977).

38. M. G. A. Lapotre, M. P. Lamb, B. McElroy, What sets the size of current ripples?. *Geology* **45**, 243–246 (2017).

39. W. F. Tanner, Ripple mark indices and their uses. *Sedimentology* **9**, 89–104 (1967).

40. S. Dumas, R. W. C. Arnott, J. B. Southard, Experiments on oscillatory-flow and combined-flow bed forms: Implications for interpreting parts of the shallow-marine sedimentary record. *J. Sediment. Res.* **75**, 501–513 (2005).

41. M. E. Brookfield, S. Silvestro, Eolian systems, in *Facies Models 4* (Geological Association of Canada, 2010), pp. 139–166.

42. G. Kocurek, J. Nielson, Conditions favourable for the formation of warm-climate aeolian sand sheets. *Sedimentology* **33**, 795–816 (1986).

43. J. Schwan, The structure and genesis of Weichselian to early hologene aeolian sand sheets in western Europe. *Sediment. Geol.* **55**, 197–232 (1988).

44. G. M. Ashley, J. B. Southard, J. C. Boothroyd, Deposition of climbing-ripple beds: A flume simulation. *Sedimentology* **29**, 67–79 (1982).

45. J. Grotzinger, J. Bell III, K. Herkenhoff, J. Johnson, A. Knoll, E. McCartney, S. McLennan, J. Metz, J. Moore, S. Squyres, R. Sullivan, O. Ahronson, R. Arvidson, B. Joliff, M. Golombek, K. Lewis, T. Parker, J. Soderblom, Sedimentary textures formed by aqueous processes, Erebus crater, Meridiani Planum, Mars. *Geology* **34**, 1085–1088 (2006).

46. D. M. Rubin, J. C. Schmidt, J. N. Moore, Origin, structure, and evolution of a reattachment bar, Colorado River, Grand Canyon, Arizona. *J. Sediment. Res.* **60**, 982–991 (1990).

47. J. R. Dingler, H. E. Clifton, Tidal-cycle changes in oscillation ripples on the inner part of an estuarine sand flat, *Mar. Geol.* **60**, 219–233 (1984).

48. G. M. Martínez, C. N. Newman, A. De Vicente-Retortillo, E. Fischer, N. O. Renno, M. I. Richardson, A. G. Fairén, M. Genzer, S. D. Guzewich, R. M. Haberle, A.-M. Harri, O. Kemppinen, M. T. Lemmon, M. D. Smith, M. de la Torre-Juárez, A. R. Vasavada, The modern near-surface Martian climate: A review of in-situ meteorological data from Viking to Curiosity. *Space Sci. Rev.* **212**, 295–338 (2017).

49. S. G. Banham, S. Gupta, D. M. Rubin, K. S. Edgett, R. Barnes, J. Van Beek, J. A. Watkins, L. A. Edgar, C. M. Fedo, R. M. Williams, K. M. Stack, J. P. Grotzinger, K. Lewis, R. C. Ewing, M. Day, A. R. Vasavada, A rock record of complex aeolian bedforms in a Hesperian desert landscape: The Stimson formation as exposed in the Murray buttes, Gale crater, Mars. *J. Geophys. Res. Planets* **126**, e2020JE006554 (2021).

50. T. F. Bristow, J. P. Grotzinger, E. B. Rampe, J. Cuadros, S. J. Chipera, G. W. Downs, C. M. Fedo, J. Frydenvang, A. C. McAdam, R. V. Morris, C. N. Achilles, D. F. Blake, N. Castle, P.

Craig, D. J. D. Marais, R. T. Downs, R. M. Hazen, D. W. Ming, S. M. Morrison, M. T. Thorpe, A. H. Treiman, V. Tu, D. T. Vaniman, A. S. Yen, R. Gellert, P. R. Mahaffy, R. C. Wiens, A. B. Bryk, K. A. Bennett, V. K. Fox, R. E. Millken, A. A. Fraeman, A. R. Vasavada, Brine-driven destruction of clay minerals in Gale crater, Mars. *Science* **373**, 198–204 (2021).

51. L. A. Edgar, J. P. Grotzinger, A. G. Hayes, D. M. Rubin, S. W. Squyres, J. F. Bell, K. E. Herkenhoff, Stratigraphic architecture of bedrock reference section, Victoria Crater, Meridiani Planum, Mars, in *Sedimentary Geology of Mars* (SEPM Special Publication No. 102, 2012), pp. 195–209.

52. K. W. Lewis, O. Aharonson, J. P. Grotzinger, S. W. Squyres, J. F. Bell III, L. S. Crumpler, M. E. Schmidt, Structure and stratigraphy of home plate from the spirit mars exploration rover. *J. Geophys. Res. Planets* **113**, E12S36 (2008).

53. J. M. Metz, J. P. Grotzinger, D. Mohrig, R. Milliken, B. Prather, C. Pirmez, A. S. McEwen, C. M. Weitz, Sublacustrine depositional fans in southwest Melas Chasma. *J. Geophys. Res. Planets* **114**, E10002 (2009).

54. P. M. Myrow, M. P. Lamb, R. C. Ewing, Rapid sea level rise in the aftermath of a Neoproterozoic snowball Earth, *Science* **360**, 649–651 (2018).

55. Coastal Engineering Research Center, Shore Protection Manual (US Army Corps of Engineers, 1984).

56. M. P. Lamb, W. W. Fischer, T. D. Raub, J. T. Perron, P. M. Myrow, Origin of giant wave ripples in snowball Earth cap carbonate. *Geology* **40**, 827–830 (2012).

57. Z.-J. You, B. Yin, A unified criterion for initiation of sediment motion and inception of sheet flow under water waves *Sedimentology* **53**, 1181–1190 (2006).

58. M. C. Malin, M. A. Ravine, M. A. Caplinger, F. Tony Ghaemi, J. A. Schaffner, J. N. Maki, J. F. Bell III, J. F. Cameron, W. E. Dietrich, K. S. Edgett, L. J. Edwards, J. B. Garvin, B. Hallet, K. E. Herkenhoff, E. Heydari, L. C. Kah, M. T. Lemmon, M. E. Minitti, T. S. Olson, T. J. Parker, S. K. Rowland, J. Schieber, R. Sletten, R. J. Sullivan, D. Y. Sumner, R. A. Yingst, B. M. Duston, S.

M. Nair, E. H. Jensen, The Mars Science Laboratory (MSL) mast cameras and descent imager: Investigation and instrument descriptions. *Earth Space Sci.* **4**, 506–539 (2017).

59. S. Le Mouélic, O. Gasnault, K. E. Herkenhoff, N. T. Bridges, Y. Langevin, N. Mangold, S. Maurice, R. C. Wiens, P. Pinet, H. E. Newsom, R. G. Deen, J. F. Bell III, J. R. Johnson, W. Rapin, B. Barraclough, D. L. Blaney, L. Deflores, J. Maki, M. C. Malin, R. Perez, M. Saccoccio, The ChemCam Remote Micro-Imager at Gale crater: Review of the first year of operations on Mars. *Icarus* **249**, 93–107 (2015).

60. J. Maki, D. Thiessen, A. Pourangi, P. Kobzeff, T. Litwin, L. Scherr, S. Elliott, A. Dingizian, M. Maimone, The Mars Science Laboratory engineering cameras. *Space Sci. Rev.* **170**, 77–93 (2012).

61. F. J. Calef III, T. Parker, MSL Gale Merged Orthophoto Mosaic, PDS Annex, U.S. Geological Survey (2016); https://astrogeology.usgs.gov/search/map/mars_msl_gale_merged_orthophoto_mosaic_25cm.

62. F. J. Calef, T. Soliman, H. E. Abarca, S. P. Abercrombie, M. W. Powell, Multi-mission geographic information system: An open source solution for planetary science operation, in *4th Planetary Data Workshop* (Lunar and Planetary Institute, 2019), p. 7071.

63. A. S. McEwen, E. M. Eliason, J. W. Bergstrom, N. T. Bridges, C. J. Hansen, W. Alan Delamere, J. A. Grant, V. C. Gulick, K. E. Herkenhoff, L. Keszthelyi, R. L. Kirk, M. T. Mellon, S. W. Squyres, N. Thomas, C. M. Weitz, Mars reconnaissance orbiter's high resolution imaging science experiment (HiRISE). *J. Geophys. Res. Planets* **112**, E05S02 (2007).

64. H. Tennekes, J. L. Lumley, *A First Course in Turbulence* (MIT Press, 1972).

65. P. D. Komar, *Beach Processes and Sedimentation* (Prentice Hall, 1998).

66. F. Pedocchi, M. H. García, Ripple morphology under oscillatory flow: 2. Experiments. *J. Geophys. Res. Oceans* **114**, C12015 (2009).

67. L. Braat, M. Z. M. Bückner, E. Sefton-Nash, M. P. Lamb, Gravity-driven differences in fluvial sediment transport fluxes on Mars and Earth. *J. Geophys. Res. Planets* **129**, e2023JE007788 (2024).

68. J. B. Southard, L. A. Boguchwal, Bed configurations in steady unidirectional water flows: 3. Effects of temperature and gravity. *J. Sediment. Petrol.* **60**, 680–686 (1990).

69. M. H. García, Sediment transport and morphodynamics, in *Sedimentation Engineering; Processes, Measurements, Modeling, and Practice* (American Society of Civil Engineers, 2008), pp. 21–163.

70. M. P. Lamb, J. Grotzinger, J. B. Southard, N. Tosca, Were ripples on Mars formed by flowing brines?, in *Sedimentary Geology on Mars* (SEPM Special Publication No. 102, 2012), pp. 139–150.

71. R. W. C. Arnott, J. B. Southard, Exploratory flow-duct experiments on combined-flow bed configurations, and some implications for interpreting storm-event stratification. *J. Sediment. Petrol.* **60**, 211–219 (1990).

72. J. H. Nienhuis, J. T. Perron, J. C. T. Kao, P. M. Myrow, Wavelength selection and symmetry breaking in orbital wave ripples, *J. Geophys. Res. Earth* **119**, 2239–2257 (2014).

73. J. C. Harms, J. B. Southard, R. G. Walker, Structures and sequences in clastic rocks: Society of Economic Paleontologists and Mineralogists Short Course Notes No. 9 (1982), pp. 2–55.